

1
2
3
4
5
6
7
8
9
10
11
12
13
14
15
16
17
18
19
20
21
22
23
24
25

Diamondized carbon nanoarchitectures as electrocatalytic material for sulfate-based oxidizing species electrogeneration

Karla Caroline de Freitas Araújo¹, Elisama Vieira dos Santos¹, Mattia Pierpaoli²,
Mateusz Ficek², José Eudes L. Santos¹, Carlos A. Martínez-Huitle^{1,*} Robert
Bogdanowicz^{2,*}

¹*Instituto de Química, Universidade Federal do Rio Grande do Norte, Natal, Rio Grande do Norte, Brazil.*

²*Faculty of Electronics, Telecommunications and Informatics, Gdańsk University of Technology, 11/12 G. Narutowicza St, 80-233 Gdańsk, Poland*

*Corresponding author's e-mail:

carlosmh@quimica.ufrn.br (C.A. Martínez-Huitle),

rbogdan@eti.pg.edu.pl (Robert Bogdanowicz)

26 **Abstract**

27 The introduction of nanotechnology seems to be an imperative factor to intensify the synergic
28 effects of electrocatalytic materials to produce strong oxidant species or to increase the active
29 sites on their surfaces as well as to enhance the conversion yield in a fuel cell, high-added
30 value products, electrolytic treatment for environmental protection or the detection limit in
31 electroanalysis. Recently, a new type of 3D-diamond electrodes was developed with boron-
32 doped carbon nanowalls (B:CNW), which was manufactured using the microwave plasma-
33 assisted chemical vapor deposition (CVD) process, improving the charge transfer and
34 enhancing the electrochemical performance. The applicability of a BDD/boron-doped carbon
35 nanowalls (BDD/B:CNW) anodes to degrade organic pollutants has been already
36 investigated; however, no attempts at the electrosynthesis of oxidizing species using these
37 diamond-carbon nanostructures have been reported yet. Therefore, the electrosynthesis of
38 sulfate-based oxidizing species was studied here to answer relevant questions from both
39 fundamental and practical point-of-view. The results demonstrated that persulfate was
40 efficiently produced at the BDD plate, while that the ion-radical sulfate could be the most
41 important oxidant at BDD/B:CNW anode when compared to other electrocatalytic materials,
42 including BDD surfaces. Persulfate concentrations ranged from 3 to 6 μM , depending on the
43 applied current density (2.5, 5.0, and 15 mA cm^{-2}), at diamond electrodes. A dye-model
44 pollutant - methyl orange (MO) was degraded below the limit of detection within 45 min
45 using BDD/B:CNW when *in-situ* sulfate-based oxidizing species were electrogenerated.
46 These kinds of 3D-diamond-carbon nanostructures are thus promising as novel
47 electrocatalyst for various catalytic applications in the environmental and energy fields.

48

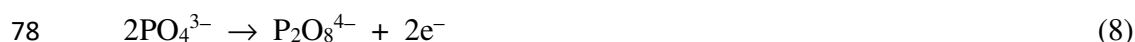
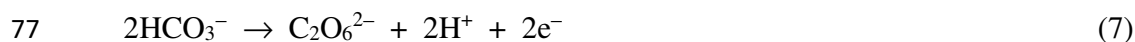
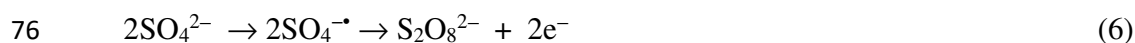
49 *Keywords:* boron-doped diamond electrode, sulfate-based oxidizing species, diamond-
50 carbon nanoarchitectures, electrocatalyst, electrogeneration.

51 1. Introduction

52 The scientific community has shown a preference to apply EO as an environment-friendly
53 electrochemical process because of its uncomplicatedness and acceptance among the
54 electrochemical advanced oxidation processes (EAOPs), in terms of electrolytic technology,
55 amenability, environmental compatibility, automation, no reagents use, renewable energies-
56 driven and in-situ production of higher concentration of oxidants [1]. In the last decades, EO
57 has competently demonstrated its effectiveness to mineralize different organic compounds in
58 a great variety of water matrices or wastewaters [2]. Nevertheless, the extension of
59 mineralization/degradation of these pollutants and their concentration as well as the type of
60 the electrogenerated oxidants strongly depends on the operating parameters and the nature of
61 the anode electrocatalytic material [3,4].

62 Various electrodes have been used in EO, like Ir-, Pt-, Ru-, Ti-, Pb- and Sn- oxide-based
63 anodes as well as synthetic diamond films [5,6]. However, boron-doped diamond (BDD)
64 anodes are considered the most effective electrocatalytic materials for
65 degrading/mineralizing refractory/priority pollutants and waterborne agents [1,2,7–9]. It is
66 due to their effective *in-situ* production of oxidizing agents, at higher concentrations, mainly
67 reactive oxygen species (ROS) (Eq. (1)-(5)) [9]. Also, peroxodisulfate ($S_2O_8^{2-}$),
68 peroxodicarbonate ($C_2O_6^{2-}$) and peroxodiphosphate ($P_2O_8^{4-}$) can be electrochemically
69 formed with ROS from the oxidation of sulfate or bisulfate by Eq. (6), bicarbonate by Eq. (7)
70 and phosphate by Eq. (8) at the BDD surface [10,11].





79 As already scientifically stated, the effective electrosynthesis of oxidizing species requires
80 an electrode with a large surface area, high electrocatalytic activities, long-term stability, as
81 well as a low cost of materials [5,12]. Thus, the introduction of nanoarchitectures seems to
82 be an essential factor to intensify the synergic effects of electrocatalytic materials to produce
83 strong oxidant species or to increase the active sites on their surfaces [13]. Novel
84 nanostructured materials can exhibit better electrochemical properties than their bulk
85 counterparts with a specific pore dimension distribution and well-defined structure-
86 morphology, maximizing the exposed-surface area and minimizing the mass transport
87 phenomena [14–16]. Thus, the advances in the preparation of highly sophisticated
88 electrocatalytic nanomaterials may lead to further improvements in the mineralization of
89 organic pollutants as well as the electrosynthesis of oxidants, making them suitable for smart
90 water solutions [17]. These technologies will play a key role in achieving the Sustainable
91 Development Goal 6 (SDG6) since these represent a substantial opportunity if their
92 implementation is carried out to guarantee sustainability and increase competence in water
93 management (to treat and distribute water for human use) [18].

94 Recently, a versatile electrode was discovered, called the “3D-nanostructured BDD/B:CNW”
95 anode. This 3D-diamondized-carbon nanostructure possesses extraordinary electrochemical
96 properties (e.g., peculiar morphology, specific surface area and the larger extends of exposed



97 edges with a greater number of functional groups and chemisorbed heteroatoms, in particular,
98 oxygen), allowing a higher reactivity of the carbonaceous nanostructure for environmental,
99 fuel and sensors applications, compared to 2D-BDD electrode [19–21]. However, no
100 information concerning the effectiveness of this 3D-nanostructured BDD/B:CNW anode to
101 electrogeneration oxidants has been reported yet. Thus, for the first time, the electrosynthesis
102 of sulfate-based oxidants species has been studied by using a 3D-nanoarchitected
103 BDD/B:CNW anode to answer relevant questions from both fundamental and practical point-
104 of-view. An organic model compound was also chosen to prove the oxidative efficiency of
105 *in-situ* $S_2O_8^{2-}$ electrogeneration when compared with other electrode materials. The results
106 are discussed considering the existing literature on nanostructured electrodes for
107 electrocatalytic advanced oxidation processes.

108

109 **2. Materials and Methods**

110 **2.1. Materials**

111 All reagents were of analytical grade and used without further purification. The water was
112 obtained from purified water (Milli-Q system, with resistivity $\geq 18 \text{ M}\Omega \text{ cm}$ at 25 °C). Methyl
113 orange (MO) purity was 95% and it was used as received.

114

115 **2.2. Synthesis and characterization of BDD/B:CNW**

116 BDD and BDD/BCNW were synthesized using the MWPECVD system (SEKI Technotron
117 AX5400S, Japan). Thin films were grown on niobium substrates for a total of 5 h, resulting
118 in 3 μm of thickness. The detailed parameters of the thin film synthesis can be found
119 elsewhere, for BDD [ref1] and for the BDD:BCNW in Pierpaoli et al [ref2, ref3] ~~BCNW in~~
120 ~~Siuздak et al. [22], Dettlaff et al. [23], and Sobaszek et al. [24]~~ . The surface characteristics

121 of the BDD/B:CNW was carried out using a Hitachi model TM 3000 top microscope with a
122 high sensitivity semiconductor backscattered electron detector to obtain scanning electron
123 microscopy (SEM) images, using a significant magnification and operating at 15 kV voltage
124 acceleration with a tungsten filament. The SEM images were taken under a vacuum at
125 controlled temperatures and the energy dispersive X-ray (EDS) spectrum was obtained to
126 analyze the concentrations of the elements in the diamond-carbon nanostructures. Raman
127 spectra were recorded in the 50–3200 cm^{-1} range, upon excitation by a 532 nm laser; the
128 spectral resolution was equal to 2.9 cm^{-1} , in the range of 50–2000 cm^{-1} and 2.4 cm^{-1} in the
129 range of 2000–3200 cm^{-1} with an integration time of 5 s (20 averages), with a diffraction
130 grating of 300 lines/ mm^2 .

131 **2.3. Electrochemical measurements**

132 Experiments were carried out in a conventional three-electrode system in Pyrex material
133 with a capacity of 10 mL, and measurements were performed between 0.0 and +1.8 V at 10
134 mV s^{-1} for quasi-steady polarization curves in 0.05 M of Na_2SO_4 . BDD and BDD/B:CNW
135 anodes have significant areas in cm^2 , however, an exposed geometric area of ca. 0.075 cm^2
136 was used as the working electrode for electrochemical measurements, while this area was
137 increased for bulk electrolysis (see next subsection). A platinum wire and an Ag/AgCl (3 M)
138 were employed as the auxiliary and reference electrodes, respectively. The electroactive
139 surface area (A_{real}) and the differential capacitance (C_{DL}) were experimentally estimated [25–
140 27], according to Eq. 1. To do that, a potential range was selected, for BDD and BDD/B:CNW
141 electrodes, where a non-Faradaic current response is registered. This range was ≈ 0.2 V
142 potential window centered on the open-circuit potential of the system. Then, cyclic
143 voltammetry (CV) measurements were conducted in static solution by sweeping the potential



144 across the non-Faradaic region and back at 9 different scan rates (0.02, 0.04, 0.06, 0.08, 0.10,
145 0.12, 0.14, 0.16, 0.18 and 0.20 V s⁻¹) at 25±1°C in 0.05 M of Na₂SO₄. For each measurement,
146 five voltammetric profiles were recorded, and the last curve was always selected to be used for
147 plotting the graphics in this work.

$$148 \quad A_{\text{real}} = \frac{C_{\text{DL}}}{C^*} = \frac{\mu\text{F}}{\frac{\mu\text{F}}{\text{real cm}^2}} = \text{cm}^2 \quad (1)$$

149 In Eq. 1, C_{DL} is the differential capacitance of the electrode-electrolyte interface and C* is
150 approximately 60 μF (real cm²)⁻¹ which is a reference value for porous materials, regardless of
151 its composition [25,27]. Experiments were performed with an Autolab
152 potentiostat/galvanostat model PGSTAT302N.

153

154 **2.4. Spectrophotometric analysis**

155 For UV-vis spectrophotometric measurements to determine the production of persulfate, a
156 Shimadzu spectrophotometer model 1800 was employed by using *in-situ* chemical oxidation
157 (ISCO) method [28,29], operating from 190 to 800 nm. A single quartz cuvette was used
158 with an optical path of 1 cm. It is important to remark that persulfate generation can be
159 followed by ISCO method without H₂O₂ interference because the analysis of absorption
160 spectra of a yellow color solution resulting from the reaction of persulfate and iodide in the
161 presence of sodium bicarbonate reveals a clear absorbance spectrum at 352 nm.

162

163 **2.5. Electrochemical determination of methyl orange concentration**

164 Electroanalytical measurements were carried out in a conventional three-electrode system in
165 Pyrex material with a capacity of 25 mL for determining MO concentrations by differential
166 pulse voltammetry (DPV) analysis. BDD anode (silicon substrate, 500 ppm of boron doping,

167 2-3 μm of thickness), with an exposed geometric area of 0.28 cm^2 , was used as the working
168 electrode, while a platinum wire and Ag/AgCl (KCl 3 M) were employed as the auxiliary
169 and reference electrodes, respectively. DPV experiments were performed with an Autolab
170 PGSTAT 320N model to establish an analytical curve by measuring different concentrations
171 of MO in 0.05 M Na_2SO_4 . Other details of the procedure are as follows: equilibration time,
172 5 s; modulation time, 0.05 s; interval time, 0.5 s; initial potential, 0 V; end potential, +1.8 V;
173 step potential, 25 mV; and modulation amplitude, 100 mV. For determining MO
174 concentration at each predetermined time during EO tests, the samples were spiked with a
175 known quantity of a standard solution, and the standard addition method was implemented.

176

177 **2.6. Bulk experiments**

178 Experiments were carried out using a bulk electrochemical cell under stirring agitation which
179 consisted of several electrodes (anodes such as BDD plate, BDD/B:CNW, TiPt, Pb/PbO₂,
180 Ti/TiO₂-nanotubes/PbO₂ and Ti as cathode, respectively) of 1.5 cm of diameter (geometrical
181 area $\approx 7.07\text{ cm}^2$). Electrolysis of 50 mL of a synthetic solution containing 0.05 M Na_2SO_4 as
182 the supporting electrolyte was performed by applying 2.5, 10, and 15 mA cm^{-2} for 150 min
183 to prepare sulfate-based oxidizing species. Sulfate concentration was chosen based on the
184 existing literature to produce a significant concentration of persulfate [29,30]. During all
185 experiments, samples of the sulfate-based oxidizing solutions were collected at the end of the
186 electrolysis, and subsequently, these were analyzed by the ISCO-spectrophotometric method,
187 determining the final sulfate-based oxidants concentration produced. For the EO of an
188 organic target compound, 25 mL of 0.05 M of Na_2SO_4 containing 10 mg L^{-1} of MO were
189 electrochemically treated by mixing with magnetic stirring for 40 min and aliquots were



190 withdrawn at predetermined times to determine chemical oxygen demand (COD) and the
191 concentration of the target pollutant by the electroanalytic procedure. COD levels were
192 measured by using pre-dosed reagents (HANNA® vials) in 2 mL samples. Samples for COD
193 determination were digested in a thermal reactor (HANNA instrument) at 150°C for 2 h.
194 Subsequently, the samples initial and final, for all oxidation tests, were analyzed on a
195 spectrophotometer (Hanna HI 83099), at 25°C.

196

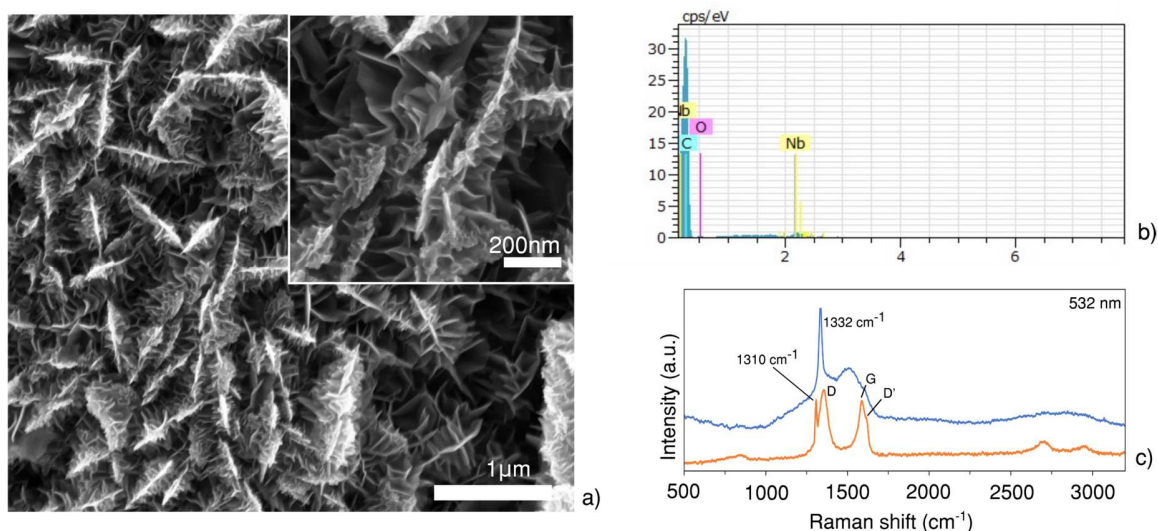
197 **3. Results and Discussion**

198 **3.1. Characterization of diamond electrode**

199 The BDD/B:CNW electrode morphology presents microscale valleys with a diameter of a
200 few micrometers, as observed in the SEM images (Fig. 1a). As previously reported [13,14,31]
201 and confirmed by SEM images; on the one hand, carbon grows vertically in form of multi-
202 layer graphene walls covered by diamond clusters. Microcavities having an opening in the
203 range between tens and hundreds of nanometres are formed between the nanowall boundaries
204 (Fig. 1a). On the other hand, “nano-flaps” also grow perpendicularly as secondary
205 protuberances to the surface of the nanowalls due to the process of synthesis [13,14,31].
206 Meanwhile, EDS spectrum evidence that the concentrations of the elements in the diamond-
207 carbon nanostructures are preferentially carbon and oxygen, confirming the BDD/B:CNW
208 composition (Fig. 1b).

209 In this context, the CVD process developed by Bogdanowicz’s group [14] is an innovative
210 approach to obtaining a carbon nanostructure with concave and convex curvatures in a simple
211 way [13,14,31]. Thus, it was possible to understand that the electrode surface and their
212 composition, as well as the density of electronic states of electrode materials [XXX], could
213 influence during the production of oxidant species. From the Raman spectra (Fig. 1c), the

214 intense peak at 1332 cm^{-1} sharply observed for the BDD sample is assigned to sp^3 -
 215 hybridized carbon, which decreases in intensity and downshift to 1310 cm^{-1} for the
 216 BDD:BCNW sample, which is typical for typical for heavily boron-doped diamond [ref],
 217 since the diborane concentration inside the reactor increases as well. Moreover, it is possible
 218 to observe the G-band at around 1580 cm^{-1} , arising from the presence of graphitic material
 219 (i.e., $\text{sp}^2\text{-C}$), and the D-band which indicates defects in graphitic structures. Finally, D' is
 220 another second-order Raman band, appearing as a shoulder peak of the G band, originating
 221 from a second-order Raman scattering at the K point, involving one iTO phonon and one
 222 defect state [ref].



223

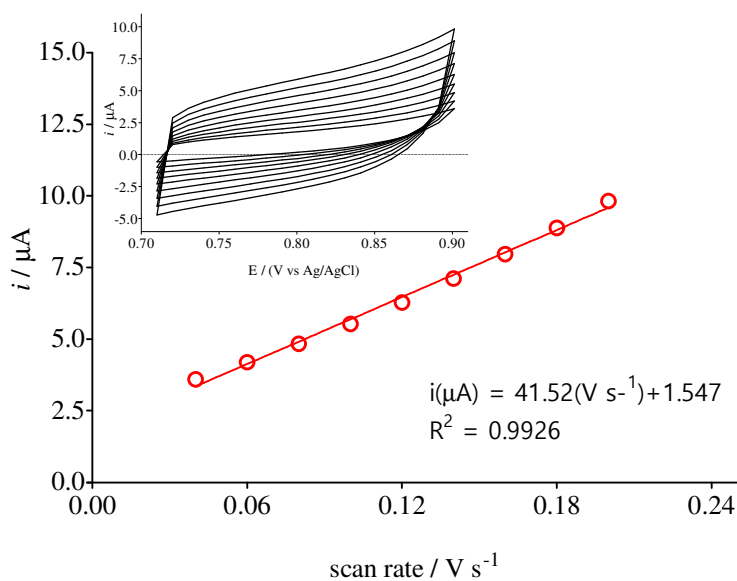
224

225 **Fig. 1.** (a) SEM images of the BDD/BCNW grown on Nb, (b) EDS spectrum, confirming the
 226 composition of BDD/BCNW electrode: C (94.42 wt.%, 97.40 at.%), O (2.90 wt.%, 2.25 at.%)
 227 and Nb (2.68 wt.%, 0.36 at.%). And (c) Raman spectra for the BDD and BDD:BCNW
 228 samples.

229

230 **3.2. Electrochemical measurements**

231 CV curves in a non-faradaic potential range were recorded at different scan rates (0.04, 0.06,
 232 0.08, 0.10, 0.12, 0.14, 0.16, 0.18 and 0.20 V s^{-1}) to estimate the electro-active surface of BDD
 233 and BDD/B:CNW electrodes. By plotting the current, which was measured in the middle of
 234 the double-layer region and recorded at different scan rates, versus the scan rate (e.g.:
 235 BDD/B:CNW, Fig. 2); a straight line was obtained, which allowed determining the double
 236 layer capacitance values for these electrocatalytic materials (Insets in Fig. 2). Then, by using
 237 the Eq. (1), the geometric area of the electrodes ($\approx 0.075 \text{ cm}^2$) and the C_{DL} values obtained
 238 ($5.40 \mu\text{F}$ and $41.52 \mu\text{F}$ for BDD and BDD/B:CNW, respectively); the real surface areas were
 239 estimated, obtaining 0.216 cm^2 and 0.692 cm^2 for BDD and BDD/B:CNW, respectively. It
 240 is important to remark that, based on existing literature data [26], reference values (C^*) for
 241 compact and porous materials should be considered to estimate the electroactive surface area,
 242 regardless of its composition. Then, $60 \mu\text{F (real cm}^2)^{-1}$ was the reference value for
 243 BDD/B:CNW, while, $25 \mu\text{F (real cm}^2)^{-1}$ for BDD plate due to the most homogeneous surface
 244 [26,27,32].



245

246 **Fig. 2.** Cyclic voltammetric (CV) analysis (from 0.04 to 0.20 V s⁻¹) to estimate the
247 capacitance for BDD/B:CNW electrode in 0.05 M of Na₂SO₄ by plotting the current values
248 in the double-layer regions as a function of scan rate. Inset: double-layer capacitance
249 measurements by using CV technique at different scan rates.

250

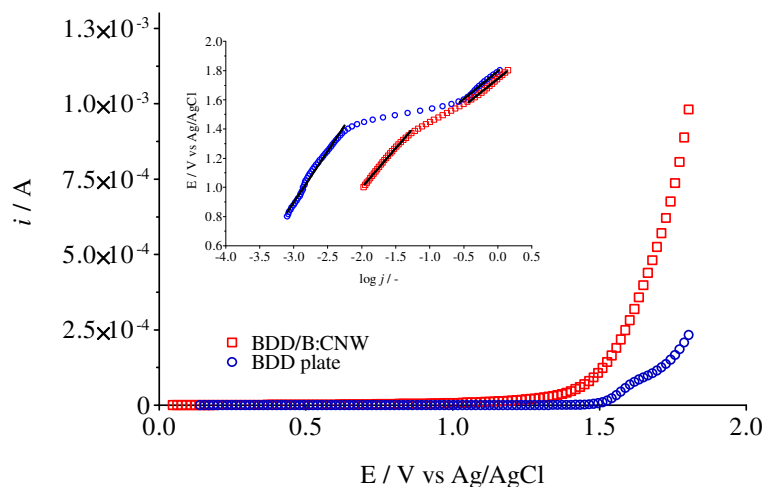
251 Although there are several methods to experimentally determine the real surface area such as
252 hydrogen adsorption, double layer capacitance, surface oxide reduction, underpotential
253 deposition of metals, and adsorbed carbon monoxide stripping [27]; for the case of BDD
254 electrodes, some approaches could be efficiently applied. However, the double-layer
255 capacitance method allows to obtain accurate surface measurements, avoiding significant
256 surface changes due to the oxygen/hydrogen evolution, formation/reduction of oxides, and
257 modification of carbon materials [27,32,33]. The double-layer capacitance also allows
258 measuring the total surface area accessible to the solution, and it is not destructive [27]. In
259 fact, in this case, the real electrode areas are superior to the geometrical value; it could be
260 due to the character of diamond surfaces, allowing for proper contact of the solution with all
261 active sites and consequently, a significant increase in the real area was achieved respect to
262 0.075 cm².

263 For BDD/B:CNW electrode, an increase in the porous properties of the material was achieved
264 due to the 3D nanostructures (see SEM images, Fig. 1) [20,21,24]; for this reason, an increase
265 in the solution contact (solution diffusion between/into the porous) could be expected [14].
266 Meanwhile, this behavior is reduced in the BDD plate due to the homogeneous surface. In
267 this context, the roughness factor ($RF = A_{\text{real}}/A_{\text{geometric}}$) was also determined for BDD and

268 BDD/B:CNW electrodes, considering the geometric surface and the estimated electroactive
269 area for each one of the electrodes, achieving values of about 2.88 and 9.22, respectively.
270 From these results, it is possible to deduce that, the new type of 3D-diamond electrodes with
271 boron-doped carbon nanowalls (B:CNW) increased its roughness by about 3.2-folds in
272 comparison to the BDD plate surface [14,15,21,34,35]. This result evidenced that, the
273 roughness controls the contact of the active sites with the solution and thus, increasing its
274 active area [14,21].

275 On the other hand, it is important to characterize the potential window and anodic
276 oxygen evolution reaction by electrochemical measurements at both carbon materials. Fig. 3
277 shows the polarization curves registered at BDD and BDD/B:CNW anodes in a sulfate
278 solution. A slight variation in the potential window is achieved, evidencing an important
279 change in the potential of the oxygen evolution reaction (OER). This behavior is mainly
280 associated with the different carbon constituents on the BDD surfaces as well as the
281 electrochemical decomposition of the supporting electrolyte [30,36,37]. Linear polarization
282 curves for BDD/B:CNW electrode showed that the potential for the OER was shifted to a less
283 positive potential (≈ 1.43 V vs Ag/AgCl). Based on previous works [36,38], it was
284 demonstrated that graphite electrode presents lower oxygen overpotential than BDD
285 electrodes, similar to the behavior achieved at BDD/B:CNW. Conversely, BDD plate showed
286 to be a poor electrocatalyst for OER, shifting this reaction to more positive potentials (Fig.
287 3).





288

289 **Fig. 3.** Polarization curves registered at BDD and BDD/B:CNW electrodes in 0.05 M of
 290 Na_2SO_4 . Inset: data in terms of Tafel plots at lower and higher overpotential regions from the
 291 potential of hydroxyl radicals' formation.

292

293 Meanwhile, additional effects could be observed when the analysis of the Tafel plots
 294 is executed. $E/\log j$ plots at both BDD electrodes are shown in the inset of Fig. 3, considering
 295 the real surface area for each one of them. As can be observed, the Tafel plots change their
 296 slope according to the lower overpotential region (<1.6 V) or high overpotential region
 297 (>1.62 V). At BDD/B:CNW, the OER seems to be the main process than that registered at
 298 BDD plate. However, no unique slope can be attributed to the Tafel plots at both BDD
 299 electrodes due to the complex set of the electrochemical reactions taking place involving
 300 most probably the OER and persulfate production. Tafel slopes about 0.6117 V decade $^{-1}$ and
 301 0.5363 V decade $^{-1}$ for BDD plate and BDD/B:CNW electrode were estimated, respectively,
 302 at lower overpotential region. Meanwhile, 0.3810 V decade $^{-1}$ and 0.3740 V decade $^{-1}$ in the



303 high overpotential region were obtained for BDD plate and BDD/B:CNW electrodes,
 304 respectively. Two distinct linearity regions can be attributed to the electrochemical reactions
 305 on the Nernst layer at BDD surface, associated with the sulfate ions in solution and water
 306 discharge, which are transformed to persulfate and hydroxyl radicals ($\cdot\text{OH}$) as well as oxygen,
 307 respectively [39,40]. From Tafel plots data as well as the current and potentials (inset of Fig.
 308 3), it is possible to infer that an important electrochemical reaction at the lower overpotential
 309 region is attained at both diamond electrodes, which could be associated with the specific
 310 interaction of sulfate ions with each one of the carbon surfaces [37,40,41].

311 Based on the existing literature [3,4,8], in the case of diamond electrodes, the
 312 mechanisms followed depend strongly on (i) extension of the oxidation of SO_4^{2-} ions at the
 313 diamond surface, via direct electron transfer, to produce persulfate (Eq. 2), (ii) the production
 314 of $\cdot\text{OH}$ at anode surface in the reaction cage (Eq. 1), (iii) the interaction of $\cdot\text{OH}$ with SO_4^{2-}
 315 ions, in the Nernst layer, to favor the production of $\text{SO}_4^{\cdot-}$ (principal intermediate) and
 316 subsequently, persulfate (Eq. 3), as well as, in some cases, the association between the sp^2 -
 317 impurities on its surface and the adsorption of SO_4^{2-} ions on these active sites to also form
 318 $\text{SO}_4^{\cdot-}$ and then, producing persulfate (Eqs. 4 and 5),



323 In the case of the BDD plate, the electrochemical reactions, which occurs at the lower
 324 overpotential region (<1.6 V), a more strong interaction is attained than that at BDD/B:CNW.

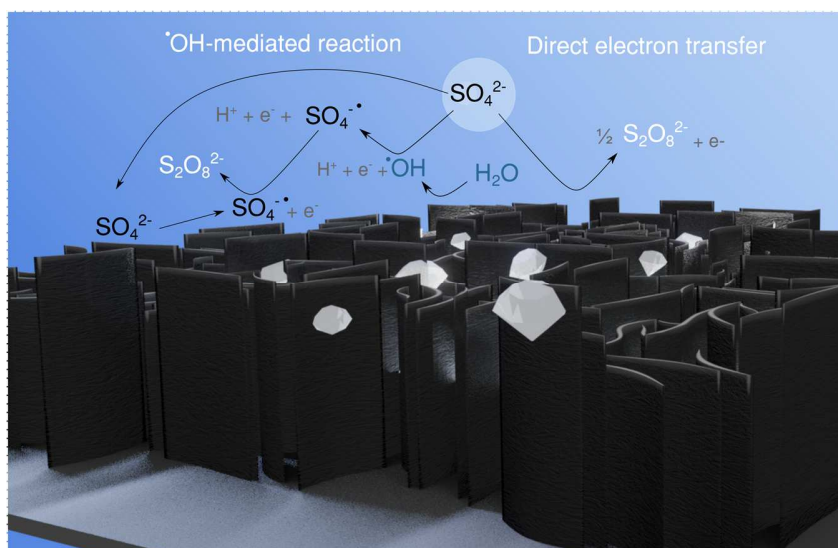
325 The Tafel slope is higher than the other one ($0.6117 \text{ V decade}^{-1}$ and $0.5363 \text{ V decade}^{-1}$, for
326 plate BDD and BDD/B:CNW electrode, respectively). These behaviors appear to be
327 associated to the production of $\text{S}_2\text{O}_8^{2-}$ or $\text{SO}_4^{\bullet-}$ at BDD surface [41], evidencing that, a direct
328 electron transfer is attained at BDD plate, in the former. While a fast-adsorptive interaction
329 of SO_4^{2-} ions on B:CNW-active sites (sp^2 -configuration) is achieved to form $\text{SO}_4^{\bullet-}$ at
330 BDD/B:CNW electrode (Eq. 8) [36]. Afterward, at both electrodes, similar surface-layer-
331 based approaches are accomplished at a higher overpotential region ($>1.6 \text{ V}$), which are
332 related to the production of $\bullet\text{OH}$ (Eq. 1) and O_2 (Eq. 6) as well as the formation of sulfate-
333 based oxidizing species (such as $\text{SO}_4^{\bullet-}$ (Eq. 3) or $\text{S}_2\text{O}_8^{2-}$ (Eq. 3 and 7)) by the participation
334 of free heterogeneous $\bullet\text{OH}$ (Eq. 3).



337 It is important to remark that, the surface-layer-based processes are achieved closer
338 to the electrode surface, in the Nernst layer (from Armstrong to nanometers), which mainly
339 depend on the diffusion distance of the free heterogeneous $\bullet\text{OH}$, the thickness of the diffusion
340 layer, the convection (agitation and flow rate) and the diffusion coefficient of SO_4^{2-} ions in
341 the solution [8]. However, the limiting steps to produce $\text{S}_2\text{O}_8^{2-}$ could be regarded as the
342 diffusion of sulfate in the diffusion layer to react with the free heterogeneous $\bullet\text{OH}$ (Eq. 3) as
343 well as the subsequent reactions at BDD ($\text{SO}_4^{\bullet-}$)-sites on diamond surface (Eq. 5).

344 For this reason, it is necessary to control the current density to stabilize the $\text{S}_2\text{O}_8^{2-}$
345 electrogenerated, determining the extension of the production of $\text{S}_2\text{O}_8^{2-}$ at both electrodes.





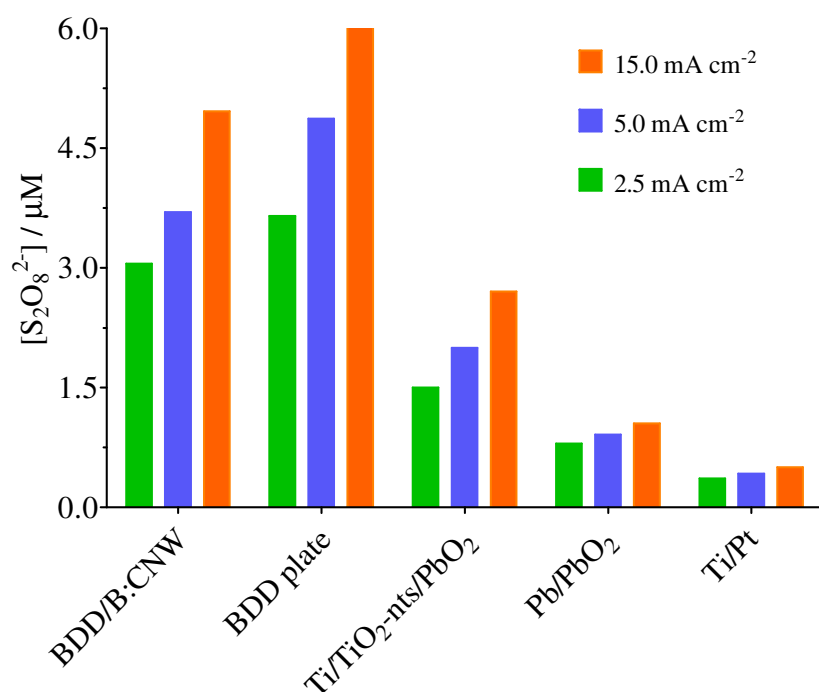
346

347 Fig xx – Schematic representation of the persulfate reaction pathway on the
 348 BDD/BCNW electrode

349

350 3.3. Electrochemical production of persulfate

351 By applying different current densities (2.5, 5.0 and 15.0 mA cm⁻²) at 25 °C, the
 352 S₂O₈²⁻ concentration produced at both electrodes was determined by ISCO method (Fig. 4).
 353 Based on the existing literature, the maximum S₂O₈²⁻ concentration is achieved between 120
 354 and 150 min of electrolysis (inset in Fig. 4), then, the final persulfate concentration was
 355 plotted for all electrocatalytic materials at different applied current densities (Figure 4).



356

357 **Fig. 4.** Electrochemically persulfate generated at different anode materials. Batch cell with
 358 50 mL of 0.05 M Na₂SO₄ at 25°C.

359 As can be observed, an increase in the concentration of persulfate was attained when
 360 the applied current density was increased (Fig. 4). For BDD plate, a significant enhancement
 361 in the production of persulfate was attained concerning those achieved at BDD/B:CNW
 362 electrode. This behavior is related to the favored mechanism to electrogenerated persulfate
 363 [8]. According to the Tafel plot analysis, a stronger interaction is attained at a lower
 364 overpotential region (<1.6 V) which indicated that the electrochemical production of S₂O₈²⁻
 365 via direct electron transfer could be attained at BDD plate [3,8]. Meanwhile, at higher
 366 potentials, the production of •OH radicals favors an enhancement of the persulfate
 367 concentration [29]. Conversely, at BDD/B:CNW anode, the production of persulfate depends

368 on the formation of $\text{SO}_4^{\cdot-}$ at BDD surface (which seems to be the main intermediate), and the
369 subsequent surface-layer-based reactions of $\text{SO}_4^{\cdot-}$ [10,37,42,42]. In this sense, the results
370 related to the quantification of persulfate concentration indicated that the extension of the
371 persulfate mechanism depends on the nature of the electrode and the j (which is directly
372 associated with the cell potential). In fact, at lower j , the increase in the persulfate
373 concentration is less significant than those achieved when higher j . For example, at BDD
374 plate, from 2.5 to 5.0 mA cm^{-2} , the persulfate concentration increases by 1.33-folds, while
375 from 5.0 to 15.0 mA cm^{-2} , it increases by 1.64-folds. Similar behavior is observed at
376 BDD/B:CNW anode, where increases of about 1.21-folds and 1.34-folds were estimated,
377 passing from 2.5 to 5.0 mA cm^{-2} , and from 5.0 to 15.0 mA cm^{-2} , respectively. However, there
378 are significant differences in the persulfate concentrations electrochemically generated.

379 Another feature that should be indicated is that a successive intensification on the j
380 could favor an increase in the production of $\cdot\text{OH}$ radicals as well as an increase in the oxygen
381 evolution reaction [43–45]. In the former, these can react with the SO_4^{2-} ions in the diffusion
382 layer to form $\text{SO}_4^{\cdot-}$ (Eq. 3); and subsequently, produce $\text{S}_2\text{O}_8^{2-}$ [42,46]. Meanwhile, when j
383 increases significantly, these can be also wasted favoring the production of O_2 (Eq. 6), in the
384 latter. These assertions are in agreement with the behavior reported by Pires *et al.* using BDD
385 electrode [36], by applying j values higher than 15 mA cm^{-2} . On the contrary, at
386 BDD/B:CNW anode, more active BDD ($\text{SO}_4^{\cdot-}$)-sites on the diamond surface can be formed
387 by increasing the j values (Eq. 3), favoring an increase in the production of persulfate via
388 Eqs. (4) and (5).

389 To understand the fundamentals of the mechanism related to the nature of
390 electrocatalytic material, the electrogeneration of persulfate at diamond electrodes was also



391 compared to TiPt, Pb/PbO₂ and Ti/TiO₂-nanotubes/PbO₂. As can be observed at Fig. 4, it is
392 evident that S₂O₈²⁻ is efficiently produced at both diamond electrodes, by applying different
393 *j*, with respect to the other anodic materials. This enhancement in the persulfate
394 electrosynthesis is due to the mechanisms associated with the anodic surfaces used as well
395 as the extension of each one of them.

396 Primarily, it is important to remark that no similar production of •OH radicals, via
397 water discharge, is attained at all electrocatalytic materials due to their active and non-active
398 nature. Then, following this statement [1,35], higher production of •OH radicals implies
399 higher production of persulfate. For example, Ti/Pt produced lower concentrations of S₂O₈²⁻
400 (0.36, 0.42 and 0.5 μM at 2.5, 5.0 and 15.0 mA cm⁻², respectively) because lower
401 electrogeneration of •OH radicals was reached at its surface, limiting the electrosynthesis
402 mechanism via the participation of free heterogeneous •OH Eqs. (3), (7) and (8).

403 Conversely, at the diamond electrode (e.g.: BDD plate), the efficient production of
404 •OH radicals is attained, favoring the generation of S₂O₈²⁻ (such as 3.65, 4.87 and 7.98 μM
405 at 2.5, 5.0 and 15.0 mA cm⁻², respectively) via the formation of SO₄^{•-}.



407 Secondly, the formation of S₂O₈²⁻ via direct electron transfer and/or via (SO₄^{•-})-active
408 sites on the electrode surfaces depends on the interaction of SO₄²⁻ ions and the
409 electrocatalytic activity of each anode. In this frame, although the extension of the
410 mechanisms is not completely clear, it seems that the electrogeneration of S₂O₈²⁻, via direct
411 oxidation of SO₄²⁻, is attained at Ti/Pt surface, as the main approach, confirming that a



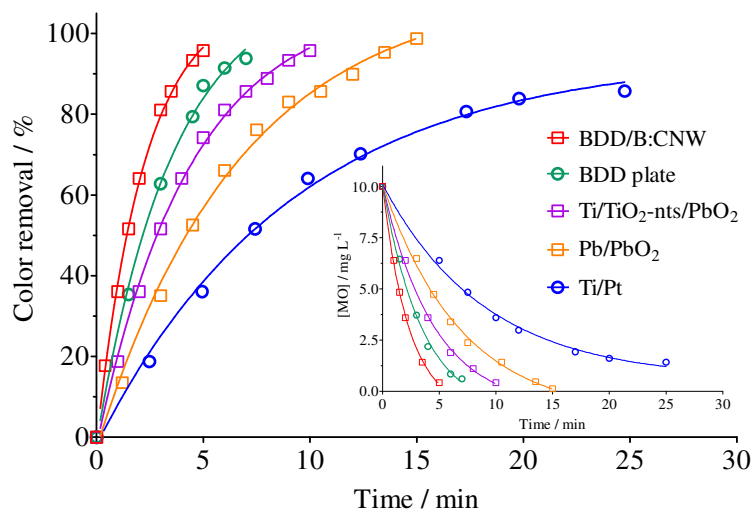
412 complex set of electrochemical and chemical reactions can be attained at non-active anodes
413 and consequently, improving the electrosynthesis yield of $S_2O_8^{2-}$ concentration.

414

415 **3.4. Electrochemical oxidation of a target organic compound**

416 To evaluate the performance of the persulfate electrochemically generated at diamond
417 surfaces and the other materials, oxidation in-situ experiments were carried out. Solutions of
418 25 mL of 0.05 M of Na_2SO_4 containing 10 mg L^{-1} of MO were electrochemically treated by
419 applying 15 mA cm^{-2} , mixing with magnetic stirring during 40 min and aliquots were
420 withdrawn at predetermined times to determine the color removal, COD decay, and the
421 concentration of the target pollutant by an electroanalytic procedure. As can be observed in
422 Fig. 5, EO process with BDD/B:CNW anode removed more than 95% of solution color in 5
423 min of electrolysis. Meanwhile, 93.8%, 95.7%, 98.6% and 85.8% were removed in 7, 10, 15
424 and 25 min at BDD plate, Ti/TiO₂-nanotubes/PbO₂, Pb/PbO₂ and TiPt, respectively.
425 According to the spectrophotometric measurements, the intensity of the visible band at 465
426 nm continuously diminished until it disappears as a function of time during the galvanostatic
427 electrolysis, leading to complete solution discoloration, in all cases. However, the absorbance
428 changes were reasonably rapid at BDD/B:CNW, BDD plate, Ti/TiO₂-nanotubes/PbO₂ and
429 Pb/PbO₂ anodes, indicating that the fragmentation of the MO chromophore group is rapidly
430 attained [29], promoting the elimination of color's solution and after that, the formation of
431 many other intermediates.



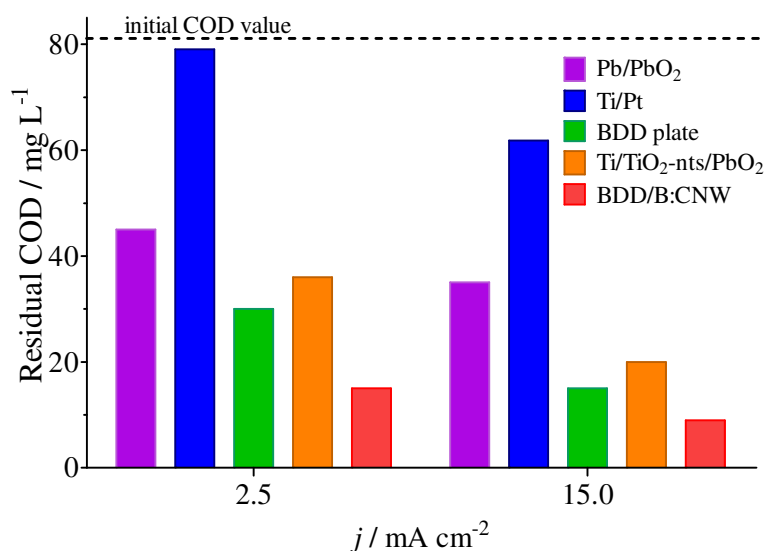


432

433 **Fig. 5.** Color removal effectiveness, as a function of time, at different anodic materials
 434 electrogenerating *in-situ* sulfate-based oxidizing species by applying 15 mA cm^{-2} at 25°C .
 435 Inset: MO concentration decay, as a function of time, under similar experimental conditions.

436 In fact, when MO concentration was followed during the EO tests, it gradually
 437 decreased and it was dependent on the nature of the material used. Again, non-active anodes
 438 were more efficient to remove MO from the solution (inset in Fig. 5), following an efficacy
 439 order as $\text{BDD/B:CNW} > \text{BDD plate} > \text{Ti/TiO}_2\text{-nanotubes/PbO}_2 > \text{Pb/PbO}_2 > \text{Ti/Pt}$. Only Ti/Pt
 440 anode was less efficient, achieving 85% of removal from the MO initial concentration.
 441 Analyzing the results obtained, BDD/B:CNW seems to be the most efficient anodic material
 442 for the elimination of organic compounds from aqueous solution via $\text{SO}_4^{2-}/\text{SO}_4^{\cdot-}/\text{S}_2\text{O}_8^{2-}$
 443 system in concomitance with free heterogeneous $\cdot\text{OH}$. However, the elimination of color and
 444 MO is not an indicator of the effective removal of organic matter. Therefore, COD removal
 445 was evaluated, at the end of the electrolysis time (40 min), by applying low and high j values

446 (2.5 and 15 mA cm⁻²). As observed in Fig. 6, different residual values of COD were
 447 determined indicating that the organic matter was oxidized in all cases.



448

449 **Fig. 6.** Residual COD values, as a function of j (2.5 and 15.0 mA cm⁻²), after 40 min of
 450 electrolysis at different anodic materials in EO tests at 25°C.

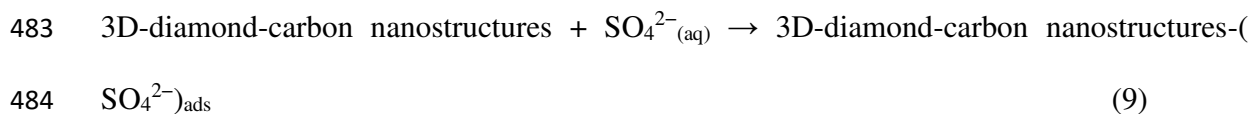
451

452 On the one hand, residual COD concentrations in solution of about 15.1 and 9.0 mg
 453 L⁻¹ were determined at 2.5 and 15 mA cm⁻² with BDD/B:CNW anode corresponding to
 454 81.80% and 89.15% of COD removals, considering 83.0 mg L⁻¹ as initial COD. On the other
 455 hand, lower COD removals (4.76% and 25.51% at 2.5 and 15 mA cm⁻², respectively) were
 456 achieved using Ti/Pt, as electrocatalytic material, that still represents a significant amount of
 457 dissolved organic matter in solution. Based on these results, it is clear that the elimination of
 458 organic matter occurred by the reactions attained in the reaction cage as surface-layer-based
 459 approaches via SO₄^{•-}, S₂O₈²⁻ and free heterogeneous [•]OH. But, the intensification of the

460 process is attained when a synergic effect is reached via the participation of all oxidant
461 species, which depends on the extension of the electrogeneration of each one of the oxidants,
462 mainly at non-active anodes.

463 The results obtained at diamond electrodes, such as the real surface area, Tafel plots,
464 persulfate production, and electrochemical degradation, evidenced that the concentration of
465 $\text{SO}_4^{\bullet-}$, $\text{S}_2\text{O}_8^{2-}$ and free heterogeneous $\bullet\text{OH}$ could be different, under the experimental
466 conditions exposed here. This hypothesis is mainly related to the efficacy to produce
467 persulfate, discoloration level, and MO decay as well as COD removal comparing both BDD
468 plate and BDD/B:CNW anodes. In the former, all parameters were efficiently achieved and
469 superior to BDD/B:CNW anode. Meanwhile, COD was significantly removed from synthetic
470 effluent at BDD/B:CNW anode than the other electrodes. This behavior could be associated
471 with the electrochemical generation of prior species that reacts in Nernst layer with the
472 organic compound before generating $\text{S}_2\text{O}_8^{2-}$. According to the literature [8,29], $\text{SO}_4^{\bullet-}$ radicals
473 are the potential candidate, as already experimental [41] and theoretically [47] established;
474 in the case of diamond electrodes, the formation of BDD-($\text{SO}_4^{\bullet-}$) sites is a pre-requisite step
475 to produce $\text{S}_2\text{O}_8^{2-}$ by recombining two $\text{SO}_4^{\bullet-}$ species (Eq. (13)). However, as already proved
476 by electrochemical measurements, this behavior is strongly dependent on the carbon sp^2 -
477 impurities content on the BDD surface. Graphitic sp^2 carbon act as the adsorption site for
478 sulfate-based species (e.g., SO_4^{2-} , HSO_4^-) at the diamond electrode, favoring the generation
479 of $\text{SO}_4^{\bullet-}$, thus producing $\text{S}_2\text{O}_8^{2-}$. In the case of BDD/B:CNW electrode, its surface was
480 meaningly enlarged due to the 3D-diamond-carbon nanostructures. These nanostructures
481 (nano-flaps, nanowalls, as well as microcavities and micro-valleys) contain a key quantity of
482 hot-spot active sites, which could participate as adsorption sulfate-based species.





486 In this context, the formation of active-($\text{SO}_4^{\bullet-}$) sites is mainly attained at BDD/B:CNW (Eq.
 487 9), producing higher concentrations of $\text{SO}_4^{\bullet-}$ at its surface when compared to the production
 488 of free heterogeneous $\bullet\text{OH}$. Although similar oxidation-reduction potentials are registered
 489 between $\text{SO}_4^{\bullet-}$ (2.5–3.1 V vs. NHE) and $\bullet\text{OH}$ (2.74 V vs. NHE), different extinction lifetimes
 490 are attained in solution, 30–40 μs for $\text{SO}_4^{\bullet-}$ and less than 1 μs for $\bullet\text{OH}$ [8], which allows to
 491 substantially improve the $\text{SO}_4^{\bullet-}$ mass transfer performances and subsequently, its contact
 492 chance and effectiveness with the pollutants in solution, as *surface-layer-* or as *volume-*
 493 *solution-* oxidation approaches [3,8,9,29,48]. Additionally, a wide pH window (from 2.0 to
 494 8.0), due to the pH adjustment, can be used to favor the efficacy of the $\text{SO}_4^{\bullet-}$ with the organic
 495 pollutants. Consequently, BDD/B:CNW produces a higher concentration of $\text{SO}_4^{\bullet-}$ that, which
 496 is available at active sites on its surface with a substantial lifetime, enhances the organic
 497 matter removal (see Fig. 6) concerning other electrodes, mainly BDD plate.

498

499 **Conclusions**

500 In summary, we can conclude that,

- 501 (i) BDD/B:CNW electrode is constituted by 3D-diamond-carbon nanostructures
 502 which increase significantly its electroactive surface area, as confirmed by the
 503 double layer capacitance determination obtaining an expansion of about 3.2-
 504 folds respect to the area of a BDD plate.



505 (ii) The roughness factor indicated that the 3D-nanomaterial increased its porous
506 properties which were also confirmed by SEM images for BDD/B:CNW
507 surface.

508 (iii) In both diamond materials, electrochemical measurements have indicated that
509 the complex set of the electrochemical reactions takes at lower and higher
510 over potential regions. However, it mainly seems that the persulfate
511 electrosynthesis depends on the stability/reactivity of $\cdot\text{OH}$ and diamond
512 surface active sites to favor the production of $\text{SO}_4^{\cdot-}$. In the case of BDD plate,
513 it produces rapidly $\text{SO}_4^{\cdot-}$, via reaction between $\cdot\text{OH}$ and SO_4^{2-} , which form
514 $\text{S}_2\text{O}_8^{2-}$, but it is a less reactive oxidizing species. Meanwhile, $\text{SO}_4^{\cdot-}$ species
515 are adsorbed at sp²-active sites at BDD/B:CNW favoring their participation
516 in the oxidation of MO.

517 (iv) In the case of PbO₂-based electrodes, indirect oxidation of SO_4^{2-} via
518 heterogeneous free $\cdot\text{OH}$ can be hypothesized where a possible formation of the
519 active-($\text{SO}_4^{\cdot-}$) sites can be also feasible at α -PbO₂ or β -PbO₂ sites, which
520 should be still completely elucidated.

521 These conclusions open a new landscape associated with the real mechanism to
522 produce sulfate-based oxidizing species at BDD anodes as well as the electrochemical
523 generation of these oxidants at other non-active and active anodes.

524

525

526

527

4. Acknowledgments

528 Financial supports from Conselho Nacional de Desenvolvimento Científico e Tecnológico
529 (CNPq, Brazil) (306323/2018-4, 312595/2019-0, 439344/2018-2), and from Fundação de
530 Amparo à Pesquisa do Estado de São Paulo (Brazil), FAPESP 2014/50945-4 and
531 2019/13113-4, are gratefully acknowledged. Carlos A. Martínez-Huitle acknowledges the
532 funding provided by the Alexander von Humboldt Foundation (Germany) and CAPES
533 (Brazil) as a Humboldt fellowship for Experienced Researcher (88881.136108/2017-01) at
534 the Johannes Gutenberg-Universität Mainz, Germany. Robert Bogdanowicz acknowledges
535 funding by the National Center for Research and Development through the Project
536 NOR/POLNOR/i-CLARE/0038/2019.

537

538

539 **5. References**

- 540 [1] C.A. Martínez-Huitle, M. Panizza, Electrochemical oxidation of organic pollutants
541 for wastewater treatment, *Curr. Opin. Electrochem.* 11 (2018) 62–71.
542 <https://doi.org/10.1016/j.coelec.2018.07.010>.
- 543 [2] C.A. Martínez-Huitle, M.A. Rodrigo, I. Sirés, O. Scialdone, C.A. Martinez-Huitle,
544 M.A. Rodrigo, I. Sire, O. Scialdone, Single and Coupled Electrochemical Processes
545 and Reactors for the Abatement of Organic Water Pollutants: A Critical Review,
546 *Chem. Rev.* 115 (2015) 13362–13407. <https://doi.org/10.1021/acs.chemrev.5b00361>.
- 547 [3] S.O. Ganiyu, C.A. Martínez-Huitle, M.A. Oturan, Electrochemical advanced
548 oxidation processes for wastewater treatment: Advances in formation and detection
549 of reactive species and mechanisms, *Curr. Opin. Electrochem.* 27 (2021).
550 <https://doi.org/10.1016/j.coelec.2020.100678>.
- 551 [4] S.O. Ganiyu, E.V. dos Santos, C.A. Martínez-Huitle, S.R. Waldvogel, Opportunities

- 552 and challenges of thin-film boron-doped diamond electrochemistry for valuable
553 resources recovery from waste: Organic, inorganic, and volatile
554 product electrosynthesis, *Curr. Opin. Electrochem.* (2021) 100903.
555 <https://doi.org/10.1016/J.COELEC.2021.100903>.
- 556 [5] G.R. Salazar-Banda, G.D.O.S. Santos, I.M. Duarte Gonzaga, A.R. Dória, K.I.
557 Barrios Eguiluz, Developments in electrode materials for wastewater treatment,
558 *Curr. Opin. Electrochem.* 26 (2021). <https://doi.org/10.1016/j.coelec.2020.100663>.
- 559 [6] D. Clematis, M. Panizza, Application of boron-doped diamond electrodes for
560 electrochemical oxidation of real wastewaters, *Curr. Opin. Electrochem.* (2021)
561 100844. <https://doi.org/10.1016/J.COELEC.2021.100844>.
- 562 [7] P.V. Nidheesh, M. Zhou, M.A. Oturan, An overview on the removal of synthetic
563 dyes from water by electrochemical advanced oxidation processes, *Chemosphere.*
564 197 (2018) 210–227. <https://doi.org/10.1016/j.chemosphere.2017.12.195>.
- 565 [8] G. Divyapriya, P. V. Nidheesh, Electrochemically generated sulfate radicals by
566 boron doped diamond and its environmental applications, *Curr. Opin. Solid State*
567 *Mater. Sci.* 25 (2021) 100921. <https://doi.org/10.1016/J.COSSMS.2021.100921>.
- 568 [9] C.A. Martínez-Huitle, E. Brillas, A critical review over the electrochemical
569 disinfection of bacteria in synthetic and real wastewaters using a boron-doped
570 diamond anode, *Curr. Opin. Solid State Mater. Sci.* 25 (2021) 100926.
571 <https://doi.org/10.1016/j.cossms.2021.100926>.
- 572 [10] K. Groenen Serrano, A critical review on the electrochemical production and use of
573 peroxy-compounds, *Curr. Opin. Electrochem.* 27 (2021) 100679.
574 <https://doi.org/10.1016/j.coelec.2020.100679>.
- 575 [11] A.S. Mora, S.T. McBeath, C.A. Cid, M.R. Hoffmann, N.J.D. Graham, Diamond

- 576 electrode facilitated electrosynthesis of water and wastewater treatment oxidants,
577 Curr. Opin. Electrochem. 32 (2022) 100899.
578 <https://doi.org/10.1016/J.COEELEC.2021.100899>.
- 579 [12] G.R. Pointer Malpass, A. de Jesus Motheo, Recent advances on the use of active
580 anodes in environmental electrochemistry, Curr. Opin. Electrochem. (2021) 100689.
581 <https://doi.org/10.1016/j.coelec.2021.100689>.
- 582 [13] X. Du, M.A. Oturan, M. Zhou, N. Belkessa, P. Su, J. Cai, C. Trelu, E. Mousset,
583 Nanostructured electrodes for electrocatalytic advanced oxidation processes: From
584 materials preparation to mechanisms understanding and wastewater treatment
585 applications, Appl. Catal. B Environ. 296 (2021) 120332.
586 <https://doi.org/10.1016/J.APCATB.2021.120332>.
- 587 [14] M. Pierpaoli, P. Jakobczyk, M. Sawczak, A. Łuczkiwicz, S. Fudala-Książek, R.
588 Bogdanowicz, Carbon nanoarchitectures as high-performance electrodes for the
589 electrochemical oxidation of landfill leachate, J. Hazard. Mater. 401 (2021) 123407.
590 <https://doi.org/10.1016/J.JHAZMAT.2020.123407>.
- 591 [15] M. Pierpaoli, M. Szopińska, B.K. Wilk, M. Sobaszek, A. Łuczkiwicz, R.
592 Bogdanowicz, S. Fudala-Książek, Electrochemical oxidation of PFOA and PFOS in
593 landfill leachates at low and highly boron-doped diamond electrodes, J. Hazard.
594 Mater. 403 (2021). <https://doi.org/10.1016/j.jhazmat.2020.123606>.
- 595 [16] S. Dutta, A. Bhaumik, K.C.W. Wu, Hierarchically porous carbon derived from
596 polymers and biomass: effect of interconnected pores on energy applications, Energy
597 Environ. Sci. 7 (2014) 3574–3592. <https://doi.org/10.1039/C4EE01075B>.
- 598 [17] B.K. Mishra, S. Chakraborty, P. Kumar, C. Saraswat, Sustainable Solutions for
599 Urban Water Security, 93 (2020). <https://doi.org/10.1007/978-3-030-53110-2>.

- 600 [18] B. Van der Bruggen, Sustainable implementation of innovative technologies for
601 water purification, *Nat. Rev. Chem.* 2021 54. 5 (2021) 217–218.
602 <https://doi.org/10.1038/s41570-021-00264-7>.
- 603 [19] M. Pierpaoli, A. Dettlaff, M. Szopińska, K. Karpienko, M. Wróbel, A. Łuczkiwicz,
604 S. Fudala-Książek, R. Bogdanowicz, Simultaneous opto-electrochemical monitoring
605 of carbamazepine and its electro-oxidation by-products in wastewater, *J. Hazard.*
606 *Mater.* 419 (2021). <https://doi.org/10.1016/j.jhazmat.2021.126509>.
- 607 [20] R. Bogdanowicz, Functionalized nanodiamonds as a perspective green carbo-catalyst
608 for removal of emerging organic pollutants, *Curr. Opin. Solid State Mater. Sci.* 26
609 (2022) 100991. <https://doi.org/10.1016/J.COSSMS.2022.100991>.
- 610 [21] R. Bogdanowicz, J. Ryl, Structural and electrochemical heterogeneities of boron-
611 doped diamond surfaces, *Curr. Opin. Electrochem.* 31 (2022) 100876.
612 <https://doi.org/10.1016/J.COELEC.2021.100876>.
- 613 [22] K. Siuzdak, M. Ficek, M. Sobaszek, J. Ryl, M. Gnyba, P. Niedziałkowski, N.
614 Malinowska, J. Karczewski, R. Bogdanowicz, Boron-Enhanced Growth of Micron-
615 Scale Carbon-Based Nanowalls: A Route toward High Rates of Electrochemical
616 Biosensing, *ACS Appl. Mater. Interfaces.* 9 (2017) 12982–12992.
617 [https://doi.org/10.1021/ACSAMI.6B16860/SUPPL_FILE/AM6B16860_SI_001.PD](https://doi.org/10.1021/ACSAMI.6B16860/SUPPL_FILE/AM6B16860_SI_001.PDF)
618 F.
- 619 [23] A. Dettlaff, P. Jakóbczyk, M. Ficek, B. Wilk, M. Szala, J. Wojtas, T. Ossowski, R.
620 Bogdanowicz, Electrochemical determination of nitroaromatic explosives at boron-
621 doped diamond/graphene nanowall electrodes: 2,4,6-trinitrotoluene and 2,4,6-
622 trinitroanisole in liquid effluents, *J. Hazard. Mater.* 387 (2020) 121672.
623 <https://doi.org/10.1016/J.JHAZMAT.2019.121672>.

- 624 [24] M. Sobaszek, K. Siuzdak, J. Ryl, M. Sawczak, S. Gupta, S.B. Carrizosa, M. Ficek,
625 B. Dec, K. Darowicki, R. Bogdanowicz, Diamond Phase (sp³-C) Rich Boron-Doped
626 Carbon Nanowalls (sp²-C): Physicochemical and Electrochemical Properties, J.
627 Phys. Chem. C. 121 (2017) 20821–20833.
628 [https://doi.org/10.1021/ACS.JPCC.7B06365/ASSET/IMAGES/MEDIUM/JP-2017-](https://doi.org/10.1021/ACS.JPCC.7B06365/ASSET/IMAGES/MEDIUM/JP-2017-063658_0016.GIF)
629 [063658_0016.GIF](https://doi.org/10.1021/ACS.JPCC.7B06365/ASSET/IMAGES/MEDIUM/JP-2017-063658_0016.GIF).
- 630 [25] S. Trasatti, Electrocatalysis: understanding the success of DSA®, *Electrochim. Acta*.
631 45 (2000) 2377–2385. [https://doi.org/10.1016/S0013-4686\(00\)00338-8](https://doi.org/10.1016/S0013-4686(00)00338-8).
- 632 [26] C. Calas-Blanchard, M. Comtat, J.L. Marty, S. Mauran, Textural characterisation of
633 graphite matrices using electrochemical methods, *Carbon N. Y.* 41 (2003) 123–130.
634 [https://doi.org/10.1016/S0008-6223\(02\)00269-5](https://doi.org/10.1016/S0008-6223(02)00269-5).
- 635 [27] M. Łukaszewski, Electrochemical Methods of Real Surface Area Determination of
636 Noble Metal Electrodes – an Overview, *Int. J. Electrochem. Sci.* 11 (2016) 4442–
637 4469. <https://doi.org/10.20964/2016.06.71>.
- 638 [28] C. Liang, C.F. Huang, N. Mohanty, R.M. Kurakalva, A rapid spectrophotometric
639 determination of persulfate anion in ISCO, *Chemosphere.* 73 (2008) 1540–1543.
640 <https://doi.org/10.1016/j.chemosphere.2008.08.043>.
- 641 [29] K.C.F. Araújo, K.N.O. Silva, M.K.S. Monteiro, D.R. da Silva, M.A. Quiroz, E.V.
642 dos Santos, C.A. Martínez-Huitle, Towards Use of Persulfate Electrogenerated at
643 Boron Doped Diamond Electrodes as Ex-Situ Oxidation Approach: Storage and
644 Service-Life Solution Parameters, *J. Electrochem. Soc.* 169 (2022) 033506.
645 <https://doi.org/10.1149/1945-7111/AC59F8>.
- 646 [30] G.O.S. Santos, K.I.B. Eguiluz, G.R. Salazar-Banda, C. Sáez, M.A. Rodrigo,
647 Understanding the electrolytic generation of sulfate and chlorine oxidative species

- 648 with different boron-doped diamond anodes, *J. Electroanal. Chem.* 857 (2020)
649 113756. <https://doi.org/10.1016/j.jelechem.2019.113756>.
- 650 [31] H. Huang, M. Yan, C. Yang, H. He, Q. Jiang, L. Yang, Z. Lu, Z. Sun, X. Xu, Y.
651 Bando, Y. Yamauchi, Graphene Nanoarchitectonics: Recent Advances in Graphene-
652 Based Electrocatalysts for Hydrogen Evolution Reaction, *Adv. Mater.* 31 (2019)
653 1903415. <https://doi.org/10.1002/ADMA.201903415>.
- 654 [32] O.A. Trasatti, S. Petri, Real surface area measurements in electrochemistry, *J.*
655 *Electroanal. Chem.* 327 (1992) 353–376.
656 [https://doi.org/https://doi.org/10.1016/0022-0728\(92\)80162-W](https://doi.org/10.1016/0022-0728(92)80162-W).
- 657 [33] J.M. Doña Rodríguez, J.A. Herrera Melián, J. Pérez Peña, Determination of the Real
658 Surface Area of Pt Electrodes by Hydrogen Adsorption Using Cyclic Voltammetry,
659 *J. Chem. Educ.* 77 (2000) 1195. <https://doi.org/10.1021/ed077p1195>.
- 660 [34] R. Bogdanowicz, A. Fabiańska, L. Golunski, M. Sobaszek, M. Gnyba, J. Ryl, K.
661 Darowicki, T. Ossowski, S.D. Janssens, K. Haenen, E.M. Siedlecka, Influence of the
662 boron doping level on the electrochemical oxidation of the azo dyes at Si/BDD thin
663 film electrodes, *Diam. Relat. Mater.* 39 (2013) 82–88.
664 [https://doi.org/https://doi.org/10.1016/j.diamond.2013.08.004](https://doi.org/10.1016/j.diamond.2013.08.004).
- 665 [35] J. Ryl, L. Burczyk, A. Zielinski, M. Ficek, A. Franczak, R. Bogdanowicz, K.
666 Darowicki, Heterogeneous oxidation of highly boron-doped diamond electrodes and
667 its influence on the surface distribution of electrochemical activity, *Electrochim.*
668 *Acta.* 297 (2019) 1018–1027. <https://doi.org/10.1016/J.ELECTACTA.2018.12.050>.
- 669 [36] J.P. De Paiva Barreto, K.C. De Freitas Araújo, D.M. De Araújo, C.A. Martínez-
670 Huitle, Effect of sp³/sp² ratio on boron doped diamond films for producing
671 persulfate, *ECS Electrochem. Lett.* 4 (2015) E9–E11.

- 672 <https://doi.org/10.1149/2.0061512eel>.
- 673 [37] T.F. Da Costa, J.E.L. Santos, D.R. da Silva, C.A. Martinez-Huitle, BDD-electrolysis
674 of oxalic acid in diluted acidic solutions, *J. Braz. Chem. Soc.* 30 (2019) 1541–1547.
675 <https://doi.org/10.21577/0103-5053.20190051>.
- 676 [38] P.K. Jiwanti, K. Natsui, K. Nakata, Y. Einaga, The electrochemical production of
677 C2/C3 species from carbon dioxide on copper-modified boron-doped diamond
678 electrodes, *Electrochim. Acta.* 266 (2018) 414–419.
679 <https://doi.org/10.1016/j.electacta.2018.02.041>.
- 680 [39] P.A. Michaud, M. Panizza, L. Ouattara, T. Diaco, G. Foti, C. Comninellis,
681 Electrochemical oxidation of water on synthetic boron-doped diamond thin film
682 anodes, *J. Appl. Electrochem.* 33 (2003) 151–154.
683 <https://doi.org/10.1023/A:1024084924058>.
- 684 [40] K. Serrano, P.A. Michaud, C. Comninellis, A. Savall, Electrochemical preparation of
685 peroxodisulfuric acid using boron doped diamond thin film electrodes, *Electrochim.*
686 *Acta.* 48 (2002) 431–436. [https://doi.org/https://doi.org/10.1016/S0013-](https://doi.org/https://doi.org/10.1016/S0013-4686(02)00688-6)
687 [4686\(02\)00688-6](https://doi.org/https://doi.org/10.1016/S0013-4686(02)00688-6).
- 688 [41] K.C. de Freitas Araújo, D.R. da Silva, E.V. dos Santos, H. Varela, C.A. Martínez-
689 Huitle, Investigation of persulfate production on BDD anode by understanding the
690 impact of water concentration, *J. Electroanal. Chem.* 860 (2020) 113927.
691 <https://doi.org/10.1016/j.jelechem.2020.113927>.
- 692 [42] Y.U. Shin, H.Y. Yoo, Y.Y. Ahn, M.S. Kim, K. Lee, S. Yu, C. Lee, K. Cho, H. il
693 Kim, J. Lee, Electrochemical oxidation of organics in sulfate solutions on boron-
694 doped diamond electrode: Multiple pathways for sulfate radical generation, *Appl.*
695 *Catal. B Environ.* 254 (2019) 156–165.

- 696 <https://doi.org/10.1016/J.APCATB.2019.04.060>.
- 697 [43] W. Wu, Z.H. Huang, T.T. Lim, Recent development of mixed metal oxide anodes
698 for electrochemical oxidation of organic pollutants in water, *Appl. Catal. A Gen.* 480
699 (2014) 58–78. <https://doi.org/10.1016/J.APCATA.2014.04.035>.
- 700 [44] M.S.M. Sillanpää, Electrode materials used for electrochemical oxidation of organic
701 compounds in wastewater, (n.d.). <https://doi.org/10.1007/s11157-017-9426-1>.
- 702 [45] M. Moradi, Y. Vasseghian, A. Khataee, M. Koby, H. Arabzade, E.N. Dragoi,
703 Service life and stability of electrodes applied in electrochemical advanced oxidation
704 processes: A comprehensive review, *J. Ind. Eng. Chem.* 87 (2020) 18–39.
705 <https://doi.org/10.1016/J.JIEC.2020.03.038>.
- 706 [46] L.W. Matzek, M.J. Tipton, A.T. Farmer, A.D. Steen, K.E. Carter, Understanding
707 Electrochemically Activated Persulfate and Its Application to Ciprofloxacin
708 Abatement, *Environ. Sci. Technol.* 52 (2018) 5875–5883.
709 https://doi.org/10.1021/ACS.EST.8B00015/SUPPL_FILE/ES8B00015_SI_001.PDF.
- 710 [47] J. Davis, J.C. Baygents, J. Farrell, Understanding Persulfate Production at Boron
711 Doped Diamond Film Anodes, *Electrochim. Acta.* 150 (2014) 68–74.
712 <https://doi.org/10.1016/j.electacta.2014.10.104>.
- 713 [48] K.N.O. Silva, K.C.F. Araújo, D.R. da Silva, C.A. Martínez-Huitle, E.V. dos Santos,
714 Persulfate-soil washing: The green use of persulfate electrochemically generated
715 with diamond electrodes for depolluting soils, *J. Electroanal. Chem.* 895 (2021)
716 115498. <https://doi.org/10.1016/j.jelechem.2021.115498>.
- 717